RSC Advances

PAPER

View Article Online
View Journal | View Issue

Open Access Article. Published on 28 September 2018. Downloaded on 7/20/2025 6:13:28 AM.
This article is licensed under a Creative Commons Attribution 3.0 Unported Licence.

Check for updates

Cite this: *RSC Adv.*, 2018, **8**, 33496

From spent alkaline batteries to $Zn_xMn_{3-x}O_4$ by a hydrometallurgical route: synthesis and characterization

Lorena Alcaraz Romo,[a] Ana López-Fernández,[a] Irene García-Díaz,[a] Paloma Fernández,[b] Ana Urbieta[b] and Félix A. López *[a]

Received 13th August 2018
Accepted 25th September 2018

DOI: 10.1039/c8ra06789a

rsc.li/rsc-advances

A series of Zn/Mn binary oxides with different molar ratios (1.4–11) were synthesized *via* co-precipitation from a solution obtained through the acidic (HCl) leaching of a black mass originating from the mechanical recycling of spent alkaline and Zn–C batteries. The oxides obtained were characterized by X-ray diffraction (XRD), Fourier-transform infrared spectroscopy (FTIR), X-ray photoelectron spectroscopy (XPS), and Raman spectroscopy. Magnetic properties of the samples were also investigated. The Raman spectroscopy results showed all the binary metallic oxides belong to the $Zn_xMn_{3-x}O_4$ ($0.25 \leq x \geq 1.75$) type. All showed a spinel crystalline structure. The saturation magnetization decreases with the Zn/Mn molar ratio; a maximum of 13.19 emu g^{-1} was found for the molar ratio of 11 at the Curie temperature (25.5 K). XPS showed that all the synthesized compounds contained Mn^{2+}, Mn^{3+} and Mn^{4+}. Mn^{2+} was the most prominent at a molar ratio of 11, Mn^{3+} was most common at a molar ratio of 2, and Mn^{4+} at 1.4.

Introduction

In recent decades, technological advances have allowed batteries to be used as energy sources in many electronic devices (toys, computers, cell phones, watches, remote controls, cameras, *etc.*).[1] Unfortunately this has led to the need to dispose of increased quantities of spent batteries.[2] The yearly global demand for batteries is currently growing at 7.7% – by 2019, battery consumption will reach 80 000 million units per year, representing a market worth US$120 billion.[3] In Spain, only about 24% of spent batteries (representing some 3031 tonnes) are currently collected for proper disposal. By 2019, however, it is expected that 65% will be recovered for recycling.[4]

The main components of batteries are manganese dioxide (positive electrode), zinc (negative electrode), an electrolyte (KOH or $ZnCl_2$ + NH_4Cl), and the steel casing. These compounds and any other heavy metals they may contain (*e.g.*, cadmium, mercury, lead, lithium) may seep out, negatively affecting the environment and human health.[4–6] These dangers, plus the elevated costs associated with the adequate management of these spent products, make the recycling of batteries an attractive option.[7]

The techniques developed for processing spent batteries fall into three groups: mechanical separation, pyrometallurgical treatment, and hydrometallurgical treatment.[8] Mechanical separation is commonly required before any further processing, especially hydrometallurgical processing. The aim is to separate the electrodes, steel casing and any plastic or paper components.[9] Mechanical separation usually involves cutting/milling, magnetic separation, dimensional separation (screening), eddy current separation (ECS) employing Foucault currents, and the final milling of the particulate fraction.[7] The result is a so-called 'black mass' (consisting largely of electrolytes, graphite, and oxides of zinc and manganese). Although pyrometallurgical treatment is the most commonly used method[10,11] hydrometallurgical treatment is gaining attention given its low cost and more environmentally friendly nature.[12]

The hydrometallurgical treatment of spent battery black mass takes place in several stages: pre-treatment, acidic or alkaline leaching, and the recovery of the Zn and Mn *via* electrolysis, liquid–liquid extraction, or selective precipitation.[13] The use of biological processes for this is also of interest since they are likely to be less environmentally harmful.[14,15] Several hydrometallurgical processes have been patented for the industrial scale recovery of Mn and Zn from spent batteries, including the Bateaux,[16] Recupyl[17] and Revabat[18] processes, among others.

Previous work performed by the present authors showed it is possible to obtain highly pure ZnO from black mass *via* leaching with ammoniacal ammonium carbonate.[19,20] This ZnO has good luminescent properties and can be used in gas sensors.[21]

[a]*Centro Nacional de Investigaciones Metalúrgicas (CENIM-CSIC), Avda. Gregorio del Amo 8, 28040 Madrid, Spain. E-mail: f.lopez@csic.es; Fax: +34-915-347425; Tel: +34-915-538-900*

[b]*Facultad de Ciencias Físicas, Universidad Complutense de Madrid, Ciudad Universitaria, Plaza de las Ciencias, 28040 Madrid, Spain*

 This journal is © The Royal Society of Chemistry 2018

Open Access Article. Published on 28 September 2018. Downloaded on 7/20/2025 6:13:28 AM.
This article is licensed under a Creative Commons Attribution 3.0 Unported Licence.

Ternary compounds of metallic oxides that contain transition metals of the AB_2O_4 type are currently a focus of research. In this context ZnO, doped with a certain amount of Mn, forms interesting spinel structures of potential use in shortwave magneto-optical[22] and spintronic devices.[23] In addition, semiconductors doped with small quantities of transition metals (TM), known as diluted magnetic semiconductors (DMS), are of great technological interest given their capacity to control spin as well as electric charge, a property that makes them potentially useful in the manufacture of new generation spintronic products.[24]

In addition, ZnO and TM doped ZnO compounds (such as Cr, Mn, V) exhibit photocatalytic applications under UV and solar radiation.[25,26] ZnO : Mn also processes the capacity to capture CO_2 and SO_2.[27] All of this makes these compounds potentially useful in several technological applications.

A number of studies have reported various ways of synthesizing the spinel $ZnMn_2O_4$. Courtel *et al.* synthesized $ZnMn_2O_4$ nanoparticles from their corresponding acetates *via* a hydrothermal process[28] and *via* coprecipitation.[29] The production of $ZnMn_2O_4$ microspheres *via* solvothermal synthesis from the corresponding acetates has been also reported.[30] Recent studies have also shown that $ZnMn_2O_4$ spinel can be obtained *via* autocombustion processes[31,32] and sol–gel methods,[33,34] among others. However, while several authors have described the recovery of different valuable metals from spent lithium ion batteries,[35–38] few of them describe in detail a comparative study of the structural characteristics and magnetic properties of these type of compounds.

The present work describes the synthesis of $Zn_xMn_{3-x}O_4$ ($0.25 \leq x \geq 1.25$) compounds with molar ratios ranging between 1.4 and 11, and with a spinel crystalline structure, *via* coprecipitation from the solution obtained following the acidic leaching of spent battery black mass.[35–38]

Experimental procedure

Preparation of black mass

Black mass produced from spent alkaline and Zn–C batteries was provided by Envirobat España, S.A (Guadalajara, Spain). Table 1 shows its mean chemical composition, as revealed by X-ray fluorescence (XRF) analysis using a PANalytical Axios wavelength dispersive spectrometer (4 kW). The mineralogical composition was determined by X-ray diffraction (XRD) using a Siemens D5000 diffractometer equipped with a Cu anode (Cu Kα radiation) and a LiF monochromator. Morphological analysis was performed by scanning electron microscopy (SEM) using a FEI Inspect microscope equipped with an X-Ray energy dispersive spectrometer (EDS).

Synthesis of zinc and manganese oxides

Different binary metallic oxides (BMO) with different proportions of Zn/Mn were produced from the black mass *via* (1) the acidic (HCl) leaching of Zn and Mn, followed by (2) the precipitation of Zn^{2+} and Mn^{2+} cations in an alkaline medium.

Table 1 Chemical composition of the starting black mass (wt%)

Compound	Black mass
Na_2O	7.75
MgO	0.23
Al_2O_3	0.46
SiO_2	1.69
P_2O_5	0.99
SO_3	0.64
Cl	1.76
K_2O	6.70
CaO	0.36
TiO_2	0.191
MnO	43.30
Fe_2O_3	1.42
Co_3O_4	0.03
NiO	0.28
CuO	0.08
ZnO	26.88
SrO	0.04
ZrO_2	0.01
Nb_2O_5	0.01
CdO	0.01
SnO_2	0.03
BaO	0.13
La_2O_3	0.05
CeO_2	0.10
PbO	0.04
C_{total}	8.20
S	0.24

Acidic leaching

100, 200, 300 or 400 g of black mass were dispersed in a 1 L suspension in 250 mL milliQ water plus 500 mL of 6 M HCl (Panreac®) and 250 mL of H_2O_2 (Panreac®). After mixing (500 rpm) for 1 h at room temperature, the suspension was filtered through a Millipore Holder filter at a pressure of 7 bars. The solid phase was discarded and the resulting filtered solutions termed L_{iq}, where q refers to the 100, 200, 300 or 400 g used. The Zn and Mn contents of these solutions were determined by atomic absorption spectroscopy (AAS) using a Varian Spectra AA 200 spectrometer. The pH of the solutions was, in all cases, approximately 0. The solutions were then subjected to precipitation in an alkaline medium.

Precipitation in an alkaline medium

The filtered solutions (L_{iq}) were subjected to a precipitation procedure involving 6 M NaOH. The pH was monitored using a pH meter at room temperature until a value between 12–14 was obtained – allowing the precipitation of zinc and manganese oxides. The solutions were then filtered, producing a solid phase of different hues of brown containing the Zn/Mn binary oxides (BMOs) and a final liquid phase (L_j) that was discarded. The solids obtained were termed BMO1, BMO2, BMO3 and BMO4 with reference to their precipitation from L1 to L4 respectively. Fig. 1 summarizes the procedure for the production of these BMOs.

Open Access Article. Published on 28 September 2018. Downloaded on 7/20/2025 6:13:28 AM.
This article is licensed under a Creative Commons Attribution 3.0 Unported Licence.

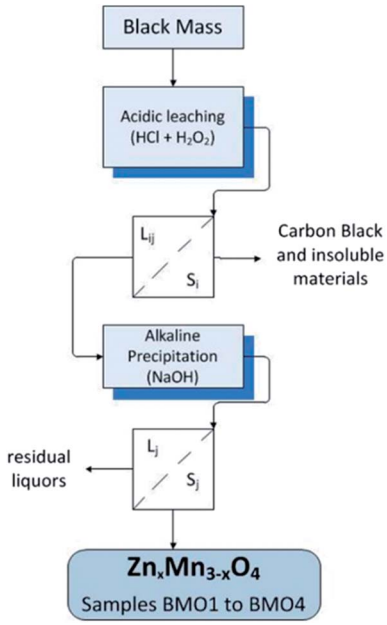

Fig. 1 Synthesis routes followed for the production of the binary metallic oxides.

Characterization of the Zn/Mn binary metallic oxides

The chemical composition of the Zn/Mn BMOs was determined by XRF using the above-mentioned PANalytical Axios wavelength dispersive spectrometer. Their mineralogical composition was determined by XRD using the above-mentioned Siemens D5000 diffractometer. The Rietveld method was used to calculate structural parameters from the XRD patterns, using TOPAS v4.2 software (Bruker ASX) and taking into account the crystallographic information for the different phases from Pearson's crystal structure database for inorganic compounds.[39] The morphology of all the BMO samples was studied by scanning electron microscopy (FE-SEM) using a JEOL JSM 7600 apparatus, as well as by transmission electron microscopy (TEM) using a JEM 2100 HT device.

Fourier-transformed infrared spectroscopy (FTIR) using a Varian 670 FTIR spectrometer (spectral range 1600–400 cm^{-1}, spectral resolution of 4 cm^{-1}) in transmittance mode was also performed. In addition, micro-Raman spectra were obtained using a confocal Horiba Jovin-Yvon LabRAM HR800 system. The samples were excited by a 633 nm He–Ne laser on an Olympus BX 41 confocal microscope with a 10× objective.

The temperature dependence of the magnetic susceptibility was measured in the 2–300 K range in a magnetic field of 1000 Oe using a Quantum Design XL-SQUID magnetometer. Hysteresis measurements were taken at 10 K with a maximum field of 5 T.

The surface chemistry of the BMO samples was examined by XPS. Spectra were recorded using a Fisons MT500 spectrometer equipped with a hemispherical electron analyzer (CLAM2) and a non-monochromatic Mg Kα X-Ray source operated at 300 W. Spectra were collected at a pass energy of 20 eV (typical for high-resolution conditions). The area under each peak was calculated after subtraction of the S-shaped background and fitting the experimental curve to a combination of Lorentzian and Gaussian lines of variable proportions. Binding energies were calibrated to the C 1s peak at 285.0 eV. The atomic ratios were computed from the peak intensity ratios and reported atomic sensitivity factors.[40]

Results and discussion

Characterization of the black mass

Table 1 shows the composition of the black mass, which consisted mainly of Mn (36.8 wt%) and Zn (23.7 wt%). The major crystalline phases were zincite (ZnO), hetaerolite ($ZnMn_2O_4$) and sylvite (KCl). Fig. 2 shows SEM images and the corresponding EDS microanalysis which reveal that the hetaerolite (Fig. 2a) and zincite (Fig. 2b) phases are present.

Synthesis of binary metallic oxides

Table 2 shows the composition of the acidic leachates. These solutions were pinkish in colour, characteristic of solutions containing Mn^{2+} ions, the intensity of the colour depending on the Mn^{2+} concentration. Eqn (1) and (2) show the dissolution reactions:[12]

$$ZnO\ (s) + 2H^+ \rightarrow Zn^{2+}\ (aq) + H_2O\ (aq) \quad (1)$$

$$ZnMn_2O_4\ (s) + 6H^+ + H_2O_2 \rightarrow Zn^{2+}\ (aq) + 2Mn^{2+}\ (aq) + 4H_2O\ (aq) + O_2\ (g) \quad (2)$$

Table 2 reveals how the Mn content decreases as the amount of dissolved black mass increases. The highest Mn content was obtained for L_{i200} sample. The concentration of Zn increases with the amount of black mass dissolved.

During the alkaline precipitation process, the precipitation of $Zn(OH)_2$ (eqn (3)) starts at pH 7.5 and increases with the pH. The precipitate was white.

$$Zn^{2+}\ (aq) + OH^-\ (aq) \rightarrow Zn(OH)_2\ (s) \quad (3)$$

$Zn(OH)_2$ (K_{sp} at 25 °C = 3×10^{-16}) continues to form until a pH of 11.5 is reached, after which (bearing in mind the amphoteric nature of this compound) it dissolves to form zincate ions (eqn (4)):

$$Zn(OH)_2\ (s) + OH^-\ (l) \rightarrow ZnO_2^{2-}\ (aq) + 2H_2O\ (aq) \quad (4)$$

The Mn^{2+} is stable up to pH 8.5, after which manganese hydroxide ($K_{ps} = 2.5 \times 10^{-13}$) is formed, along with mixed Zn/Mn hydrates (eqn (5)):

$$xZnO_2^{2-}\ (aq) + (3-x)Mn^{2+}\ (aq) + 2xOH^-\ (aq) \rightarrow Zn_xMn_{3-x}(OH)_{2x}\ (s) \quad (5)$$

These hydrated oxides are rapidly oxidized to form anhydrous oxides with a spinel structure (eqn (6)):

 This journal is © The Royal Society of Chemistry 2018

Open Access Article. Published on 28 September 2018. Downloaded on 7/20/2025 6:13:28 AM.
This article is licensed under a Creative Commons Attribution 3.0 Unported Licence.

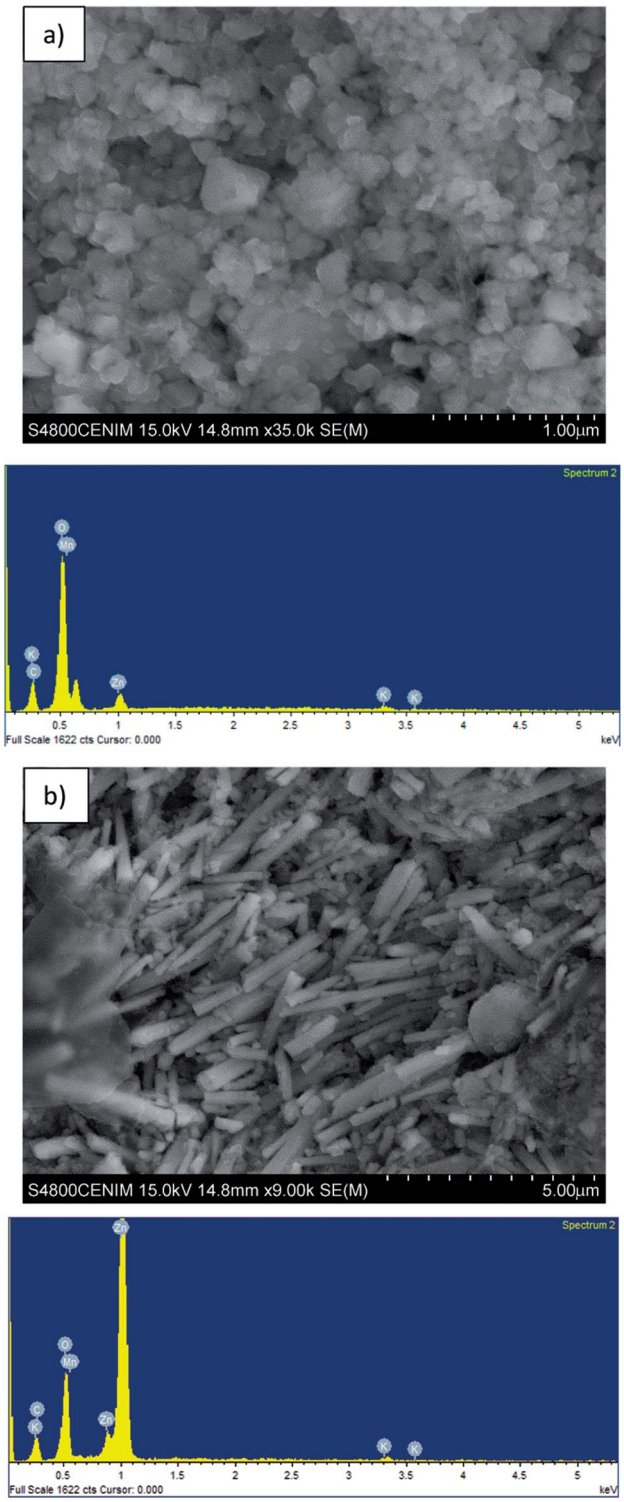

Fig. 2 SEM and EDS images of the: (a) hetaerolite, and (b) zinc oxide present in the black mass.

$$Zn_xMn_{3-x}(OH)_{2x}\ (s) + 2O_2\ (g) \rightarrow Zn_xMn_{3-x}O_4\ (s) + 2xH_2O\ (aq) \quad (6)$$

Depending on the Zn and Mn contents of each solution, the obtained value of x is different, ranging from 0.25 to 1.2. When x = 1, the product is $ZnMn_2O_4$ (sample BMO3). XRF analysis of BMO3 reveals a Zn content of 21.6 wt% and a Mn content of 49.6 wt%, similar to the stoichiometric values obtained (27.3 wt% Zn and 45.9 wt% Mn).

Ameri *et al.*[41] proposed a similar mechanism for the formation of $ZnMn_2O_4$ *via* the electrodeposition of Zn^{2+} and Mn^{2+} solutions obtained from the dissolution of zinc and manganese nitrates. In their work, the initial solutions possessed an excess of Mn^{2+} in relation to the stoichiometry of $ZnMn_2O_4$ and therefore they obtained nanostructured $ZnMn_2O_4/Mn_3O_4$. Song *et al.*[42] proposed a similar mechanism for the formation of $ZnMn_2O_4$ *via* solvothermal synthesis dissolving zinc and manganese nitrates solutions in citric acid and cetyltrimethyl ammonium bromide (CTAB).

The reactions shown above explain the formation of the Zn/Mn BMOs. In the case of BMO4 large amounts of ZnO were detected. This is a consequence of the high concentration of Zn^{2+} in the acidic solution (63.0 g L^{-1}); during the alkaline precipitation process some Zn^{2+} did not combine with the Mn^{2+}. This excess Zn^{2+} precipitated out as $Zn(OH)_2$, and later became ZnO through dehydration.

Regarding the composition, with the exception of the odd minority elements, all are composed of Zn and Mn, the exact content of each depends on the amount of solution subjected to alkaline precipitation The Zn and Mn contents and stoichiometry as determined by XRF (Table 3) and Rietveld refined XRD (Table 4) respectively agrees quite well for samples BMO1, BMO2 and BMO3. The contents Zn and Mn for BMO1 (22.8 wt% and 49.2 wt%) agrees with the stoichiometric proportion for the $Zn_{0.85}Mn_{2.15}0_4$ phase (23.4 wt% and 49.7 wt% respectively). In the case of BMO2, the Zn and Mn contents are 8.1 wt% and 66.2 wt% respectively, which agrees with the stoichiometric

Table 2 Zn and Mn content (g L^{-1}) obtained from AAS and lixiviation efficiency (%)

	Element		Lixiviation yield (%)	
Sample (acid leaching)	Zn	Mn	Zn	Mn
L_1	24.8	88.8	81.0	99.8
L_2	35.9	116.9	77.9	88.9
L_3	48.6	101.6	79.4	60.0
L_4	63.0	63.2	73.0	47.0

Table 3 XRF results for the metal binary oxides powder (expressed in %, wt/wt oxides) obtained after alkaline precipitation and extraction efficiency (%)

	Content (wt%)		Extraction efficiency (%)	
Sample	Zn	Mn	Zn	Mn
BMO1	22.8	49.2	19.2	64.3
BMO2	8.1	66.2	16.8	86.2
BMO3	26.7	46.3	46.7	72.0
BMO4	40.2	36.0	82.3	48.0

Open Access Article. Published on 28 September 2018. Downloaded on 7/20/2025 6:13:28 AM.
This article is licensed under a Creative Commons Attribution 3.0 Unported Licence.

Table 4 Mineralogical composition and calculated cell parameters of Mn/Zn binary oxides from the Rietveld refinement

Sample	Mineralogical composition (%)	Cell parameters of samples	
		a (Å)	c (Å)
BMO1	$Zn_{0.85}Mn_{2.21}0_4$ (95%)	5.756	9.266
	Impurities (5%)	—	—
BMO2	$Zn_{0.25}Mn_{2.75}0_4$ (95%)	5.766	9.393
	Impurities (5%)	—	—
BMO3	$ZnMn_20_4$ (96%)	5.758	9.240
		—	—
BMO4	$Zn_{1.25}Mn_{1.75}0_4$ (72%)		
	ZnO (12%)	5.789	8.976
	Impurities (16%)	—	—

proportion for the $Zn_{0.25}Mn_{2.75}O_4$ phase (7.1 wt% and 65.3 wt% respectively). In the case of BMO3, the agreement is also good, the Zn and Mn contents of BMO3 are 26.7 wt% and 46.3 wt% respectively, while the stoichiometry of the $ZnMn_2O_4$ phase is 27.3 wt% Zn and 45.9 wt% Mn. However, a discrepancy seems to appear for the Zn and Mn contents of BMO4, since according to stoichiometry ($Zn_{1.25}Mn_{1.75}O4$) the expected values for the contents of both elements are 29.5 wt% and 36.5 wt% respectively, while from the XRF data, the Zn content is 40.2 wt% (Table 3). Nevertheless, if we take into account the data from Table 4, in this sample, an equivalent amount of ZnO (12% wt) is detected, then accounting for the 10.7 wt% excess of Zn observed.

Characterization of the binary metallic oxides

The composition of the crystalline phases was examined by XRD. Fig. 3 shows the diffractograms recorded. In most cases, a tetragonal symmetry with a $I4_1/amd$ spatial group are obtained, which, according to JCPDS Card no. 24-1133, fits well with an spinel-type structure. However, the diffractogram for BMO4 also shows a diffraction maximum corresponding to ZnO (JCPDS Card no. 36-1451).

Table 4 shows the composition of the crystalline phases of the BMOs as determined by Rietveld refinement; where a very clear variation in the proportions of Zn and Mn is observed. The different Zn/Mn BMOs obtained also show a very high purity (95–96%).

The measured value for the a lattice parameter of the $ZnMn_2O_4$ phase is 5.758 Å, *i.e.*, slightly higher than the values reported in the literature (5.709–5.722 Å). The value for b parameter (9.240 Å), however, is much closer to previously reported values (9.222–9.238 Å).[37,41,42] The value of a parameter for the Zn/Mn BMO stoichiometries decreases with increasing Zn content. This agrees with previous results reported for $ZnMn_2O_4$ phases obtained by the ceramic method.[43]

The intensities of the diffraction maxima decrease as the Mn content increases. An increasing Mn content is therefore associated with a reduction in the crystallinity of the BMOs. Other authors have reported similar results for ZnO doped with Mn obtained *via* hydrothermal and sol–gel synthesis.[44,45]

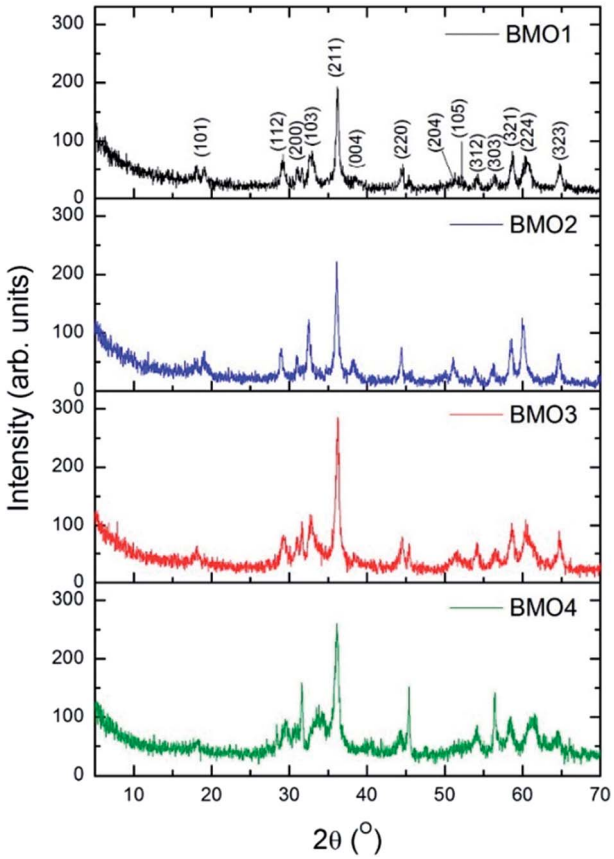

Fig. 3 X-ray diffractograms for the synthesized binary metallic oxides.

Fig. 4 shows SEM images of the different BMOs. All reveal agglomerated particles of near-spherical morphology, similar to those reported for other samples of similar composition.[46] No changes in this morphology are observed with the variation in the Zn/Mn content. Tetragonal crystals characteristic of the spinel phase are also visible (parts a and b of this figure).

Fig. 5 shows TEM images of the different BMOs. Two different morphologies are present. In BMO1, BMO2 and BMO3 samples, spherical particles are mainly observed, while in BMO4 both spherical and hexagonal-shaped particles are visible. The hexagonal shaped particles could be related to the higher content of ZnO particles[21] in agreement with our results of the Rietveld analysis (see Table 3). The mean diameter of the particles is 40, 50 and 35 nm for BMO1, BMO2 and BMO3 respectively. An increase in the Mn content leads to an increase in particle size, as previously reported.[43]

Fig. 6 shows the FTIR spectra for the BMOs. All show two main absorption bands at approximately 527 and 634 cm^{-1}. These may be respectively attributed to distortion vibration of Mn^{3+} cations in an octahedral environment, and stretching vibration at Mn–O tetrahedral sites. A weaker band is also observed at around 420 cm^{-1}, due to stretching vibration of Mn^{3+} at octahedral sites.[44–46]

Fig. 7a shows the normalized Raman spectra for the different $Zn_xMn_{3-x}O_4$ samples. In all the spectra the bands are attributable to $ZnMn_2O_4$. These results are consistent with those obtained in the XRD analysis.

Open Access Article. Published on 28 September 2018. Downloaded on 7/20/2025 6:13:28 AM.
This article is licensed under a Creative Commons Attribution 3.0 Unported Licence.

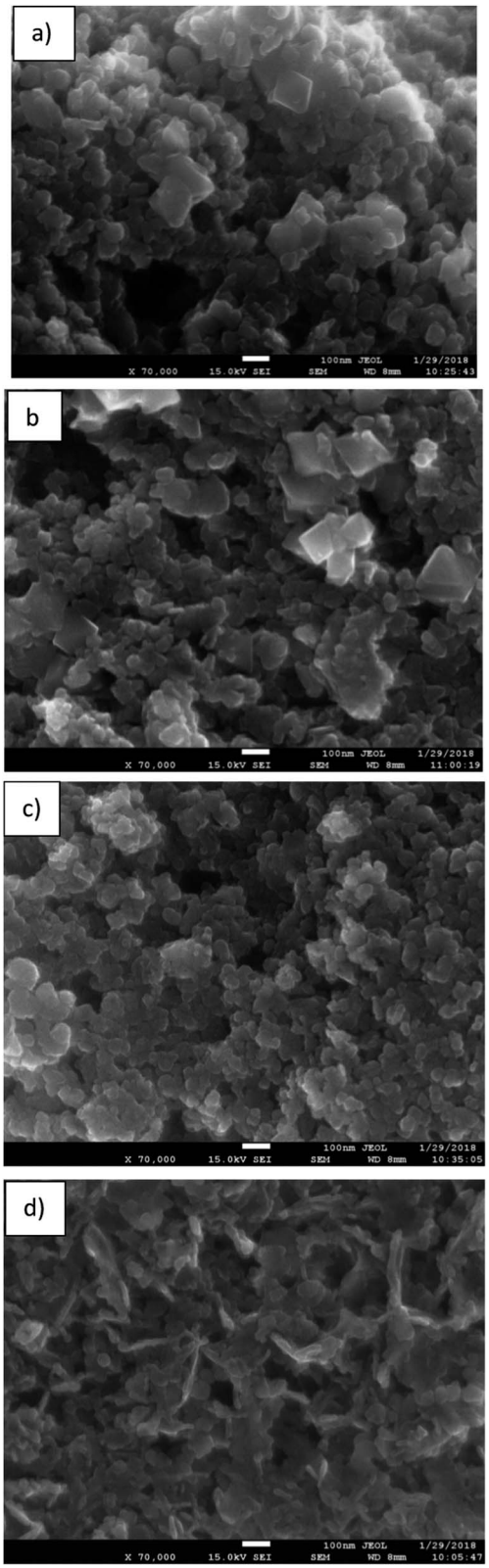

Fig. 4 SEM images of the binary metallic oxides synthesized: (a) BMO1; (b) BMO2; (c) BMO3 and (d) BMO4.

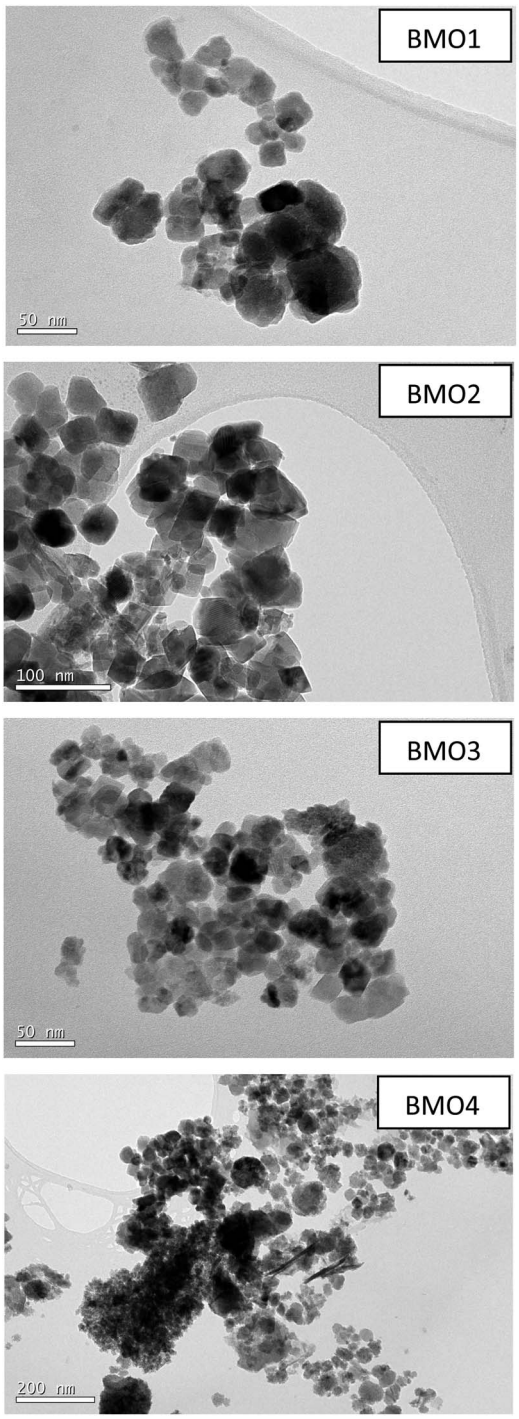

Fig. 5 TEM images of the binary metallic oxides synthesized.

According to the group theory, oxides of the stoichiometry XMn_2O_4 (where X = Zn, Mn) with a spinel-type crystalline structure and $I4_1/amd$ space group have 10 active Raman modes: $\Gamma = 2A_{1g} + 3B_{1g} + B_{2g} + 4E_g$.[47] However, the present spectra do not show all these modes; indeed, the maximum number ever observed has been seven.[48,49] The vibration modes above 600 cm^{-1}, correspond to the movement of oxygen atoms in the tetrahedral AO_4 groups, and reflect an A_{1g} symmetry.

The low frequency modes are characteristic of octahedral sites (BO_6). Other authors report a high variation in the position of the Raman peaks for $ZnMn_2O_4$. Malavasi *et al.*[48] reported peaks at 300.2, 320.5, 381.9, 475.5 and 677.6 cm^{-1}, Tortosa

Open Access Article. Published on 28 September 2018. Downloaded on 7/20/2025 6:13:28 AM.
This article is licensed under a Creative Commons Attribution 3.0 Unported Licence.

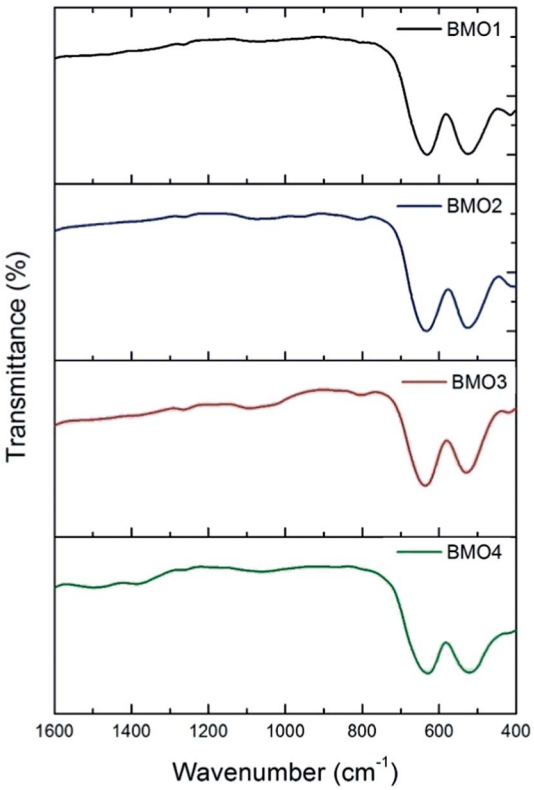

Fig. 6 FTIR spectra of the binary metallic oxides synthesized.

et al.[49] at 276, 316, 320, 369, 463, 563, 630 and 663 cm^{-1}, and Li *et al.*[50] at 171, 321, 384, 476, 635 and 677 cm^{-1}. In the present work, these peaks appear around 301, 350, 477 and 648 cm^{-1}. The band in the 645–670 cm^{-1} range might be attributed to manganese oxides and Zn/Mn complexes.[47] Fig. 7b shows a zoom of this Raman peak. Note that as the Mn content increases, the height of the peak decreases. According to XPS, in the sample with the higher Mn content, the predominant oxidation state is Mn^{2+}, hence the differences observed in the Raman peak could be explained by the substitution of Zn^{2+} by Mn^{2+} (which is larger) in the BMOs,[51] which would lead to a reduction in the bond distances. In addition, a broadening of the Raman bands can be appreciated related to the purity and crystallinity of the samples. These results are in good agreement with those obtained from the Rietveld refinement where highest percentage of impurities leading to a broader Raman bands.

Magnetic properties

Fig. 8 shows the variation in magnetic susceptibility per unit mass (χ_g) *vs.* temperature over the range 2–300 K in a 1000 Oe field. All the BMOs behave in a similar way, the magnetic susceptibility rises to a peak value and then decreases. These inflection points allow us to determine the Curie temperature (T_c) for each BMO (Table 5). As the value of x increases in the nominal composition of the $Zn_xMn_{3-x}O_4$ phases, the T_c reduces, as reported by Nádherný *et al.*[52] BMO2 shows the greatest magnetic susceptibility, in agreement with the XPS results (Fig. 9). For this sample, the majority charge state for Mn ions is +2, hence, since Mn^{2+} has the largest magnetic dipole moment (5.9μB), a largest magnetic moment and saturation magnetization are expected.

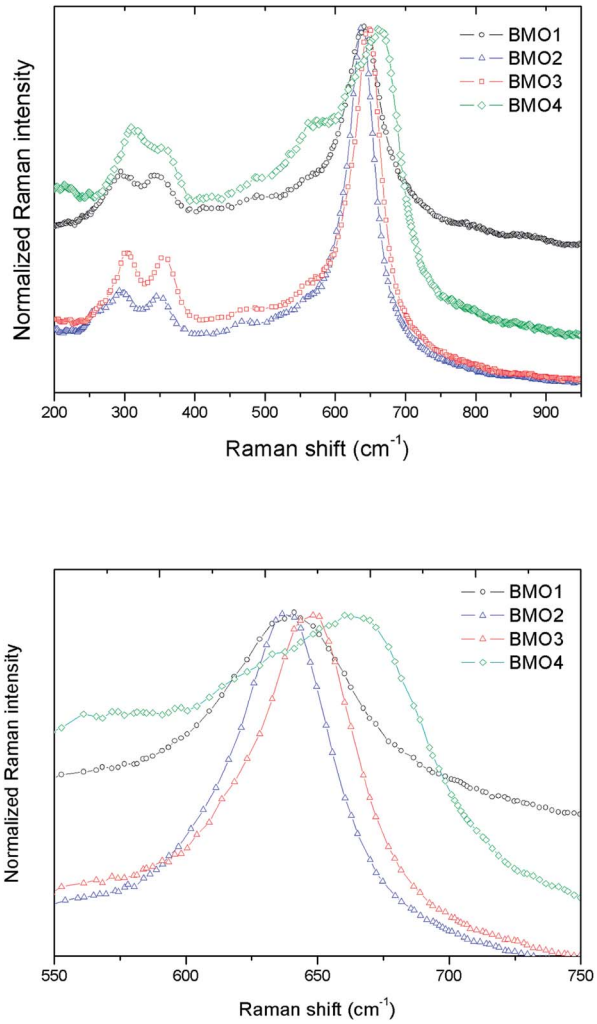

Fig. 7 (a) Normalized Raman spectra for different Zn/Mn ratios, and (b) zoom of the Raman peak in the 645–670 cm^{-1} range.

Different theories exist regarding the magnetic properties of (Zn, TM) O-type (with transition metals) oxides. Sharma *et al.*[53]

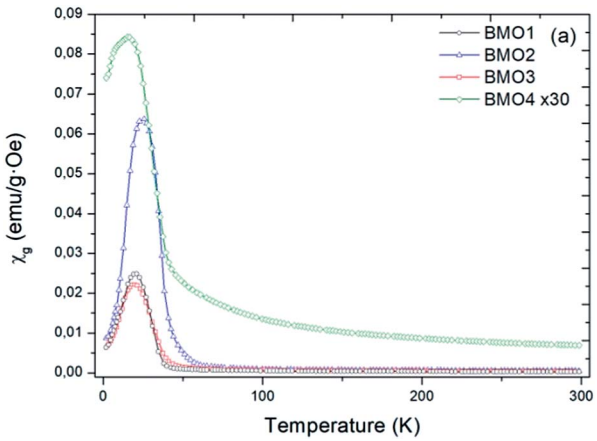

Fig. 8 Magnetic susceptibility per unit mass *versus* temperature in a field of $H = 1000$ Oe.

Open Access Article. Published on 28 September 2018. Downloaded on 7/20/2025 6:13:28 AM.
This article is licensed under a Creative Commons Attribution 3.0 Unported Licence.

Table 5 Curie temperatures (T_N), magnetization at saturation (M_s) and coercive field (H_c) for the different BMO studied

Sample	T_N (K)	M_s (emu g^{-1})	H_c (Oe)
BMO1	24.1	6.17	1720
BMO2	25.5	13.19	1720
BMO3	19.7	5.86	1220
BMO4	15.5	1.56	940

and Kundaliya *et al.*[54] explain the ferromagnetism of these materials by assuming a uniform distribution of Mn in a ZnO matrix, or through the existence of phases with a $Zn_xMn_{2-x}O_3$ stoichiometry stabilized by oxygen vacancies. Others explain it *via* the coexistence of Mn atoms in different states of oxidation.[55] Fig. 9 shows the XPS spectra for the 2p Mn structure of each BMO. The bond energies for Mn 2p3/2 of MnO, Mn_2O_3 and MnO_2 fall within the ranges 640.6–641.7, 641.7–641.9 and 641.9–642.6 eV respectively.[56,57] Table 6 shows the elemental atomic percentages for the different Zn/Mn ratios, and the percentages according to the Mn oxidation state. In all the examined BMOs, mixtures of Mn^{2+}, Mn^{3+} and Mn^{4+} are obtained. The XPS spectra for the O 1s are also shown in Fig. 9. In all cases, the obtained spectra exhibit asymmetric peaks. In this respect, there is a controversy in the interpretation of O 1s XPS spectra for different oxides. The band peaked at around 534 eV in some cases is attributable to hydroxyl groups OH, or other radicals on the sample surface[58,59] or oxygen vacancies.[60,61] For the present BMOs, none of these possibilities can be ruled out. Either, the existence of oxygen vacancies created to compensate the electric charge or the different Mn ions could be equally responsible for the magnetic behavior.

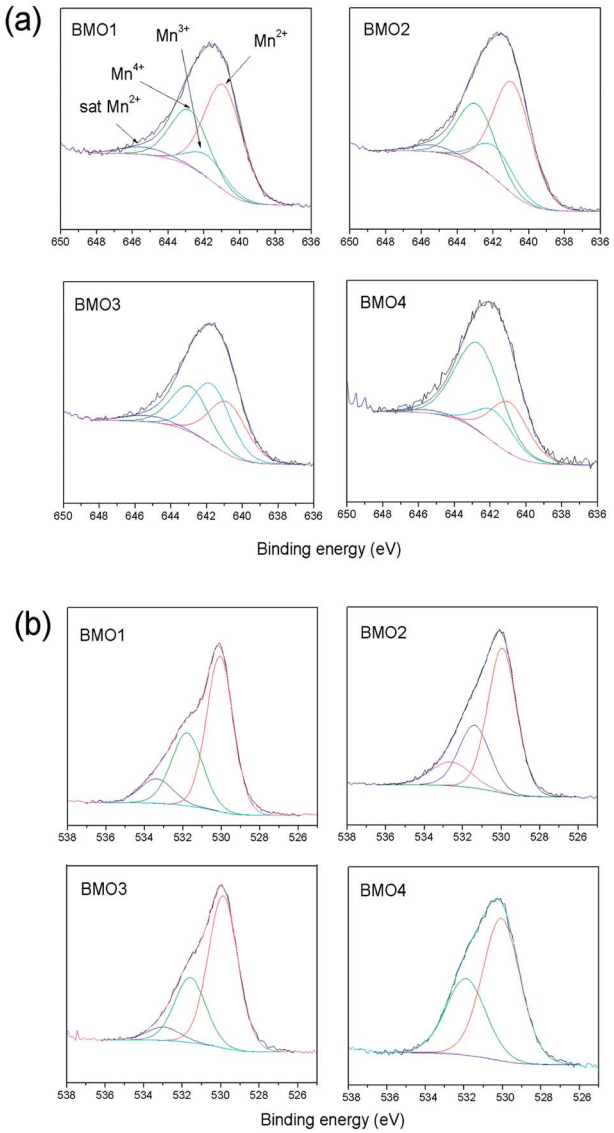

Fig. 9 (a) XPS Mn 2p spectra and (b) XPS O 1s spectra of the binary metallic oxides.

Table 6 Atomic ratio Mn/Zn calculated from the data obtained by XPS and distribution of the percentage of Mn according to the oxidation state

Sample	Atomic ratio Mn/Zn	Mn^{2+}	Mn^{3+}	Mn^{4+}
BMO1	8.3	14.5	3	7.8
BMO2	12.2	15.4	4.4	8.5
BMO3	1.3	6.3	7.3	5.5
BMO4	0.6	3.4	2.1	7.1

Fig. 10 shows the magnetization curves *versus* applied field. All are representative of a ferromagnetic material with magnetic domains. As expected, the magnetic saturation (M_s) increased with the Mn content, reaching a value of 13.2 emu g^{-1} for BMO2. Table 5 shows the different M_s values obtained for the BMOs in a coercive field (H_c). M_s decreases with increasing Zn content, a consequence of the presence of its non-magnetic cations.[52] This was particularly clear for BMO4, which has the lowest Zn/Mn ratio and Mn mainly in the Mn^{4+} oxidation state (as determined by XPS). Thus – in agreement with other authors who have studied spinel BMOs of $Zn_xMn_{3-x}O_4$ stoichiometry[52] – the magnetic properties of the present BMOs can be explained according to a model of nanometric-scale ferrimagnetic clusters of Mn_3O_4 in an antiferromagnetic $ZnMn_2O_4$ matrix.[62,63] These results are in good agreement with previous studies on

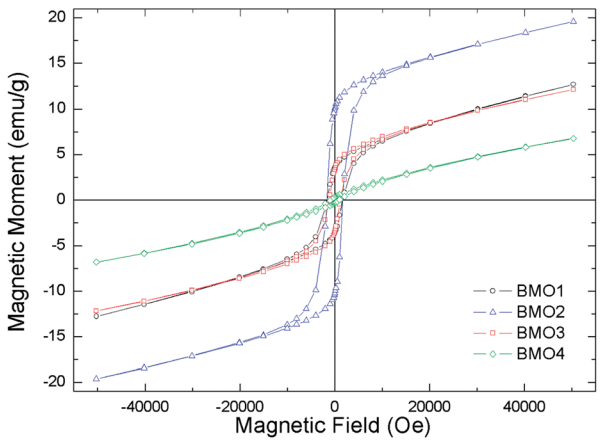

Fig. 10 Magnetization curves in the applied magnetic field at a temperature of 10 K.

Open Access Article. Published on 28 September 2018. Downloaded on 7/20/2025 6:13:28 AM.
This article is licensed under a Creative Commons Attribution 3.0 Unported Licence.

$Zn_xMn_{3-x}O_4$ phases formed by members of Mn_3O_4 and $ZnMn_2O_4$. The Mn_3O_4 phase contains Mn in oxidation state II at tetrahedral positions, and in state III at octahedral positions. As the Zn content increases (with increasing x in the stoichiometry $Zn_xMn_{3-x}O_4$), the tetrahedral sublattice occupied by Mn^{2+} begins to be occupied by Zn^{2+}. Table 6 shows how, in most cases, an increase in x is accompanied by a reduction in Mn^{2+} and an increase in Mn^{3+}. The existence of Mn^{4+} can be explained by the presence, in some samples, of MnO_2-type impurities (detected during Rietveld refinement analysis) or oxygen vacancies, as suggested by Kundaliya *et al.*[54]

Conclusions

The present work reports the synthesis and characterization of different Zn/Mn BMOs from the black mass of spent Zn/C and alkaline batteries. The XRD patterns of most of these BMOs show diffractions maxima attributable to tetragonal symmetry s.g. $I4_1/amd$ and a spinel-type type structure. The Rietveld refinement results reveal phases of $Zn_xMn_{3-x}O_4$ stoichiometry with magnetic properties explainable *via* a model of nanoscale clusters of ferrimagnetic Mn_3O_4 in an antiferromagnetic $ZnMn_2O_4$ matrix. All the BMOs contain Mn^{2+}, Mn^{3+} and Mn^{4+}. The synthesis described provides a simple method to obtain $Zn_xMn_{3-x}O_4$compounds useful potential for several applications. This process would appear to be a good way to obtain spinel from spent batteries – an useful product from a dangerous waste.

Conflicts of interest

The authors declare no conflict of interest.

Acknowledgements

Lorena Alcaraz was funded by the Comunidad de Madrid *via* a Postdoctoral Grant (Ref. PEJD-2016/AMN-2314) contract co-financed by the European Social Fund. Ana López Fernández was funded by the Comunidad de Madrid *via* a Junior Technical Grant (Ref. PEJ15/AMB/Al-0049) contract co-financed by the European Social Fund. This work has been partially supported by MINECO/FEDER (MAT2015-65274-R).

Notes and references

1 E. Sayilgan, T. Kukrer, F. Ferella, A. Akcil, F. Veglio and M. Kitis, *Hydrometallurgy*, 2009, **97**, 73–79.
2 V. J. Inglezakis and K. Moustakas, *J. Environ. Manage.*, 2015, **150**, 310–321.
3 B. University, *Global Battery Markets*, http://batteryuniversity.com/learn/article/global_battery_markets.
4 A. M. Bernardes, D. C. R. Espinosa and J. A. S. Tenório, *J. Power Sources*, 2004, **130**, 291–298.
5 D. Pant and T. Dolker, *Waste Manag.*, 2017, **60**, 689–695.
6 S. Karnchanawong and P. Limpiteeprakan, *Waste Manag.*, 2009, **29**, 550–558.
7 T. Buzatu, G. Popescu, I. Birloaga and S. Sâceanu, *Waste Manag.*, 2013, **33**, 699–705.
8 A. Sobianowska-Turek, W. Szczepaniak and M. Zabłocka-Malicka, *J. Power Sources*, 2014, **270**, 668–674.
9 P. Gasper, J. Hines, J.-P. Miralda, R. Bonhomme, J. Schaufeld, D. Apelian and Y. Wang, *J. New Mater. Electrochem. Syst.*, 2013, **16**, 297.
10 E. Sayilgan, T. Kukrer, N. O. Yigit, G. Civelekoglu and M. Kitis, *J. Hazard. Mater.*, 2010, **173**, 137–143.
11 G. Belardi, R. Lavecchia, F. Medici and L. Piga, *Waste Manag.*, 2012, **32**, 1945–1951.
12 S. Abid Charef, A. M. Affoune, A. Caballero, M. Cruz-Yusta and J. Morales, *Waste Manag.*, 2017, **68**, 518–526.
13 F. Ferella, I. De Michelis, F. Beolchini, V. Innocenzi and F. Vegliò, *Int. J. Chem. Eng.*, 2010, **2010**, 659434.
14 M. V. Gallegos, L. R. Falco, M. A. Peluso, J. E. Sambeth and H. J. Thomas, *Waste Manag.*, 2013, **33**, 1483–1490.
15 M. J. Kim, J. Y. Seo, Y. S. Choi and G. H. Kim, *Waste Manag.*, 2016, **51**, 168–173.
16 C. Lindermann Walter and C. H. Siblingen, Process for the recovery of raw materials from presorted collected waste, especially scrap electrochemical batteries and accumulators, *US Pat.* 5575907, 1996.
17 F. Tedjar, Recycling used electric cells by hydrometallurgical treatment, Int. Patent Appl., WO 021708 A3, 13 March, 2003.
18 A. Serstevens, Method for recycling and treating of salt and alkaline batteries, European Patent Application, EP 1148571, 2001.
19 F. A. López, T. Cebriano, I. García-Díaz, P. Fernández, O. Rodríguez and A. L. Fernández, *J. Cleaner Prod.*, 2017, **148**, 795–803.
20 T. Cebriano, I. García-Díaz, A. L. Fernández, P. Fernández and F. A. López, *J. Environ. Chem. Eng.*, 2017, **5**, 2903–2911.
21 C. Sardá, G. Escalante, I. García-Díaz, F. A. López and P. Fernández, *J. Mater. Sci.*, 2018, **53**, 2026–2033.
22 A. A. Othman, M. A. Osman, E. M. M. Ibrahim, M. A. Ali and A. G. Abd-Elrahim, *Mater. Sci. Eng., B*, 2017, **219**, 1–9.
23 V. M. De Almeida, A. Mesquita, A. O. De Zevallos, N. C. Mamani, P. P. Neves, X. Gratens, V. A. Chitta, W. B. Ferraz, A. C. Doriguetto, A. C. S. Sabioni and H. B. De Carvalho, *J. Alloys Compd.*, 2016, **655**, 406–414.
24 Q. Q. Gao, Q. X. Yu, B. Chen and H. Zhu, *J. Alloys Compd.*, 2014, **590**, 446–452.
25 M. A. Mahmood, S. Baruah and J. Dutta, *Mater. Chem. Phys.*, 2011, **130**, 531–535.
26 R. Ullah and J. Dutta, *J. Hazard. Mater.*, 2008, **156**, 194–200.
27 A. A. Davydov, V. I. Marshneva and M. L. Shepotko, *Appl. Catal., A*, 2003, **244**, 93–100.
28 F. M. Courtel, Y. Abu-Lebdeh and I. J. Davidson, *Electrochim. Acta*, 2012, **71**, 123–127.
29 F. M. Courtel, H. Duncan, Y. Abu-Lebdeh and I. J. Davidson, *J. Mater. Chem.*, 2011, **21**, 10206.
30 W. Dang, F. Wang, Y. Ding, C. Feng and Z. Guo, *J. Alloys Compd.*, 2017, **690**, 72–79.
31 M. Abdollahifar, S. S. Huang, Y. H. Lin, Y. C. Lin, B. Y. Shih, H. S. Sheu, Y. F. Liao and N. L. Wu, *J. Power Sources*, 2018, **378**, 90–97.

Open Access Article. Published on 28 September 2018. Downloaded on 7/20/2025 6:13:28 AM.
This article is licensed under a Creative Commons Attribution 3.0 Unported Licence.

32 M. Y. Nassar, E. A. El-Moety and M. F. El-Shahat, *RSC Adv.*, 2017, **7**, 43798–43811.
33 T. Zhang, Y. Gao, H. Yue, H. Qiu, Z. Guo, Y. Wei, C. Wang, G. Chen and D. Zhang, *Electrochim. Acta*, 2016, **198**, 84–90.
34 M. Zhao, S. Chen, X. Chang, L. Dong and Y. Yin, *Ceram. Int.*, 2016, **42**, 16349–16353.
35 A. V. M. Silveira, M. P. Santana, E. H. Tanabe and D. A. Bertuol, *Int. J. Miner. Process.*, 2017, **169**, 91–98.
36 J. Ordoñez, E. J. Gago and A. Girard, *Renewable Sustainable Energy Rev.*, 2016, **60**, 195–205.
37 W. S. Chen, C. T. Liao and K. Y. Lin, *Energy Procedia*, 2017, **107**, 167–174.
38 J. Qu, Y. Feng, Q. Zhang, Q. Cong, C. Luo and X. Yuan, *J. Alloys Compd.*, 2015, **622**, 703–707.
39 P. Villars and K. Cenzual, 2009.
40 C. D. Wagner, L. E. Davis, M. V. Zeller, J. A. Taylor, R. H. Raymond and L. H. Gale, *Surf. Interface Anal.*, 1981, **3**, 211–225.
41 B. Ameri, S. S. H. Davarani, H. R. Moazami and H. Darjazi, *J. Alloys Compd.*, 2017, **720**, 408–416.
42 M. S. Song, Y. J. Cho, D. Y. Yoon, S. Nahm, S. H. Oh, K. Woo, J. M. Ko and W. Il Cho, *Electrochim. Acta*, 2014, **137**, 266–272.
43 B. Hadžić, N. Romčević, M. Romčević, I. Kuryliszyn-Kudelska, W. Dobrowolski, U. Narkiewicz and D. Sibera, *Opt. Mater.*, 2016, **58**, 317–322.
44 M. Ristić, S. Musić, S. Popović, D. Dragčević, M. Marciuš and M. Ivanda, *J. Mol. Struct.*, 2013, **1044**, 255–261.
45 K. M. Anilkumar, M. Manoj, B. Jinosha, V. S. Pradeep and S. Jayalekshmi, *Electrochim. Acta*, 2017, **236**, 424–433.
46 P. T. M. Bui, J.-H. Song, Z.-Y. Li, M. S. Akhtar and O.-B. Yang, *J. Alloys Compd.*, 2017, **694**, 560–567.
47 W. G. Fateley, N. T. McDevitt and F. F. Bentley, *Appl. Spectrosc.*, 1971, **25**, 155–173.
48 L. Malavasi, P. Galinetto, M. C. Mozzati, C. B. Azzoni and G. Flor, *Phys. Chem. Chem. Phys.*, 2002, **4**, 3876–3880.
49 M. Tortosa, F. J. Manjón, M. Mollar and B. Marí, *J. Phys. Chem. Solids*, 2012, **73**, 1111–1115.
50 H. Li, B. Song, W. J. Wang and X. L. Chen, *Mater. Chem. Phys.*, 2011, **130**, 39–44.
51 R. D. Shannon, *Acta Crystallogr., Sect. A: Cryst. Phys., Diffr., Theor. Gen. Crystallogr.*, 1976, **32**, 751–767.
52 L. Nádherný, M. Maryško, D. Sedmidubský and C. Martin, *J. Magn. Magn. Mater.*, 2016, **413**, 89–96.
53 M. K. Sharma, R. N. Gayen, A. K. Pal, D. Kanjilal and R. Chatterjee, *J. Alloys Compd.*, 2011, **509**, 7259–7266.
54 D. C. Kundaliya, S. B. Ogale, S. E. Lofland, S. Dhar, C. J. Metting, S. R. Shinde, Z. Ma, B. Varughese, K. V. Ramanujachary, L. Salamanca-Riba and T. Venkatesan, *Nat. Mater.*, 2004, **3**, 709–714.
55 F. Rubio-Marcos, A. Quesada, M. A. García, M. A. Bañares, J. L. G. Fierro, M. S. Martín-Gonzalez, J. L. Costa-Krämer and J. F. Fernández, *J. Solid State Chem.*, 2009, **182**, 1211–1216.
56 O. A. Bulavchenko, Z. S. Vinokurov, T. N. Afonasenko, P. G. Tsyrul'nikov, S. V. Tsybulya, A. A. Saraev and V. V. Kaichev, *Dalton Trans.*, 2015, **44**, 15499–15507.
57 G. C. Allen, S. J. Harris, J. A. Jutson and J. M. Dyke, *Appl. Surf. Sci.*, 1989, **37**, 111–134.
58 D. R. Mullins, S. H. Overbury and D. R. Huntley, *Surf. Sci.*, 1998, **409**, 307–319.
59 K.-D. Schierbaum, *Surf. Sci.*, 1998, **399**, 29–38.
60 A. Q. Wang, P. Punchaipetch, R. M. Wallace and T. D. Golden, *J. Vac. Sci. Technol., B: Microelectron. Nanometer Struct.–Process., Meas., Phenom.*, 2003, **21**, 1169.
61 M. Naeem, S. K. Hasanain, M. Kobayashi, Y. Ishida, A. Fujimori, S. Buzby and S. I. Shah, *Nanotechnology*, 2006, **17**, 2675–2680.
62 K. Dwight and N. Menyuk, *Phys. Rev.*, 1960, **119**, 1470–1479.
63 D. P. Shoemaker, I. S. Abumohor, E. E. Rodriguez, T. Proffen and R. Seshadri, *Phys. Rev. B*, 2009, **80**, 9.